ISET Journal of Earthquake Technology, Paper No. 580, Vol. 60, No. 3, September 2023, pp. 75–99

ATTENUATION OF THE PEAKS OF EARTHQUAKE GROUND MOTION ALONG THE HIMALAYAN OROGENIC BELT

I.D. Gupta (Corresponding author)
Independent Scholar, Row House 4, Suncity, Pune 411051, India
E mail *id: idgrh4@gmail.com*

M.D. Trifunac
Dept. of Civil Engineering, Univ. of Southern California, Los Angeles, California 90089
E mail id: *misha.trifunac@gmail.com*

ABSTRACT

Empirical prediction relationships have been developed for the peak accelerations, velocities and displacements for five different combinations of earthquake sources and the regions of recording along Himalayan orogenic belt with widely differing source-to-site path attenuation characteristics. Due to a limited number of strong motion records available, a specially devised regression analysis has been carried out to develop these relationships. The predicted values have been shown to be in good agreement with the recorded data and to be physically realistic on seismological grounds and other independent measurements like stress drop and Q-parameter. These prediction models specific to local earthquakes recorded in the Northwest Himalayan (NWH) region, the Northeast India (NEI) region and the National Capital Region (NCR) of India, and the distant earthquakes in the Indo-Burmese subduction (IBS) and Hindu Kush Subduction (HKS) zones recorded in the NEI and NWH regions, respectively, will provide a basis for hazard mapping of several different quantities of interest in these regions derived from one or more of the peaks of the earthquake ground motion.

KEYWORDS: Peaks of ground motion along the Himalayan orogenic belt; Peak strains in the ground caused by earthquake waves; Correction of response spectra for differential ground motion

INTRODUCTION

The recorded strong motion data in India is very limited and pertains mainly to the Himalayan region. This data has been used in the past by a number of investigators (e.g.; Sharma et al., 2009; Anbazhagan et al., 2013; Raghukanth and Kavitha, 2014; Raghucharan et al., 2019; Ramkrishnan et al. 2021; etc.) to develop empirical ground motion prediction relations for 5% damped response spectral acceleration ordinates.

The purpose of this paper is to present the scaling and attenuation equations of peak accelerations, velocities, and displacements based on recorded earthquake ground motions along the Himalayan orogeny (Figure 1a). The results are intended to complement the scaling equations for the Fourier and response spectral amplitudes, which we developed for the same regions (Figure 1b; Gupta and Trifunac 2017, 2018 a, b, c, 2019). Peak accelerations can be used for traditional scaling of design spectra and knowledge of all three peak parameters to generate the complete response spectrum (Malhotra 2006). Peak velocities will be used for the extension of response spectral amplitudes at short periods, for large-in-plan and high-frequency (stiff) structures (Trifunac and Todorovska 1997; Trifunac and Gičev 2006), and for deterministic and probabilistic estimates of strains in the soil (Todorovska and Trifunac 1996 a, b, Trifunac et al. 1996; Trifunac and Lee 1996). Peak displacements can be used to evaluate the contribution of cord rotations to the response of tall structures with large plan dimensions (Trifunac et al. 2020) and for a probabilistic fault displacement hazard analysis (Todorovska et al. 2007; Gupta, 2024).

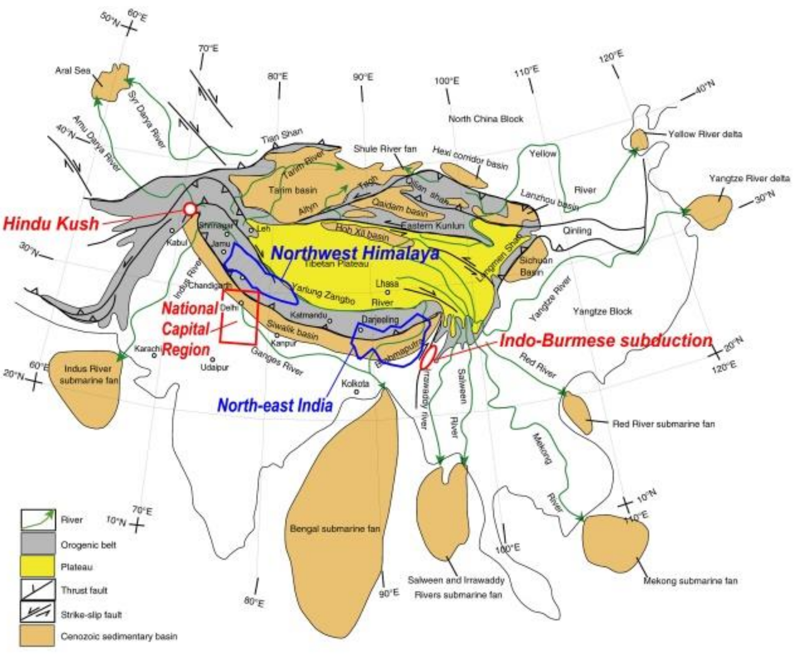

Fig. 1a A geotectonic map of the Tibetan Plateau with adjacent areas (orogenic belt, Cenozoic sedimentary basins, major river systems, and their submarine fans; modified from Wang et al. 2014). Also shown are: (1) the deep earthquake sources in the Hindu Kush, (2) the earthquake regions of Western Himalaya and Northeast India (enclosed by irregular lines), (3) the deep earthquakes in the Indo-Burmese subduction zone, and (4) the National Capital Region of India, where small earthquakes occur near Delhi

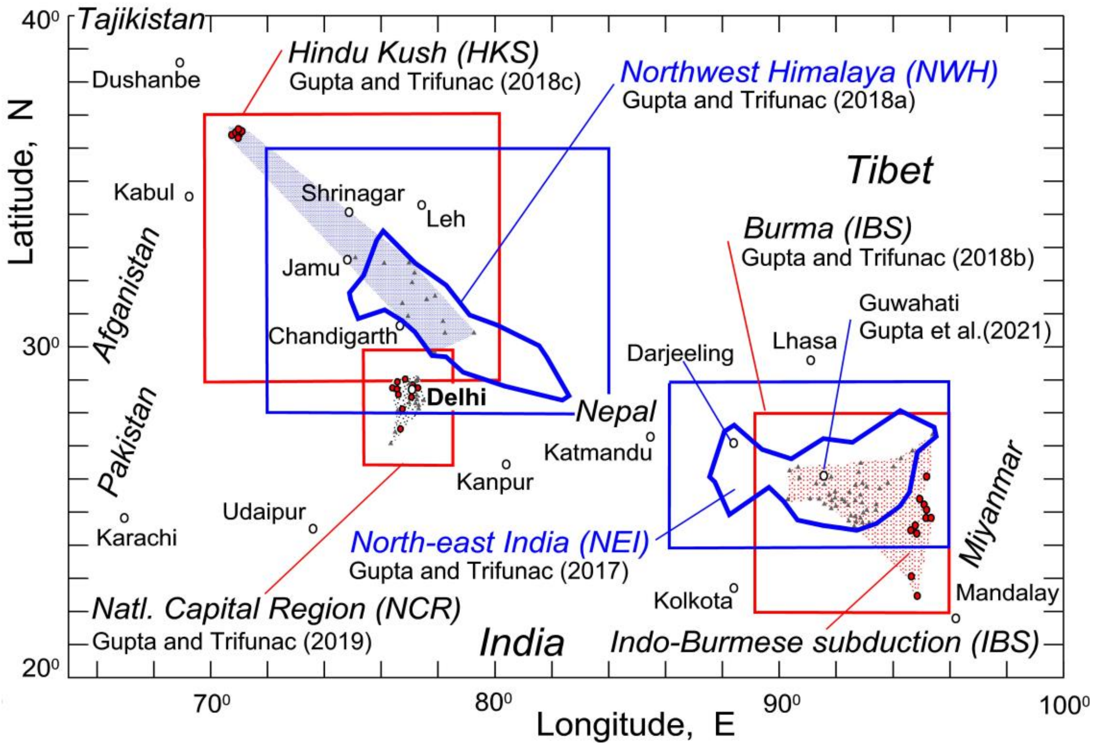

Fig. 1b Spatial relationships among the regions where we have previously analyzed attenuations of strong motion spectral amplitudes. The squares cover areas of epicenters and of the recording stations in the Hindu Kush, Western Himalaya region, the National Capital Region of India, Northeast India, and the Indo-Burmese subduction zone (Gupta and Trifunac 2017, 2018 a, b, c, 2019)

Before the age of digital computers, only the amplitudes of uncorrected peak accelerations (Trifunac and Brady 1975, 1976) could be correlated with earthquake magnitude or site intensity. Following the 1971 earthquake in San Fernando, California, and the systematic digitization and processing of strong motion accelerograms (Hudson 1979), it became possible to develop advanced empirical scaling of spectral amplitudes. Since that time numerous studies of strong ground motion have been and continue to be published (Douglas 2003, 2017; Douglas and Aochi 2008).

STRONG MOTION DATA

The uniformly processed strong motion data utilized in this study has been described in detail in Gupta (2018), which includes 485 three-component digital records from PESMOS site (http://www.pesmos.in) and 146 analog records from Chandrasekaran and Das (1993) and Shrikhande (2001). The available data has been grouped into five different combinations of earthquake source zones and regions of recording that represent five different source-to-site path attenuation characteristics. These are local earthquakes recorded in the Northwest Himalayan (NWH) region, local earthquakes recorded in the Northeast India (NEI) region, local earthquakes recorded in the National Capital Region (NCR) of India, the Indo-Burmese subduction (IBS) earthquakes recorded in NEI region zone and large earthquakes in HKS region recorded in NWH region, as shown in Figure 1b and described in detail in the papers cited in this figure. For brevity, we refer to the five cases considered simply as the NWH, NEI, NCR, IBS and HKS regions. The distributions with respect to epicentral distance, earthquake magnitude, and focal depth of the three-component strong motion records available in each of the five regions are shown in Figure 2. In general, the distance range of recording is seen to increase with an increase in magnitude, but the distribution with respect to depth is somewhat random.

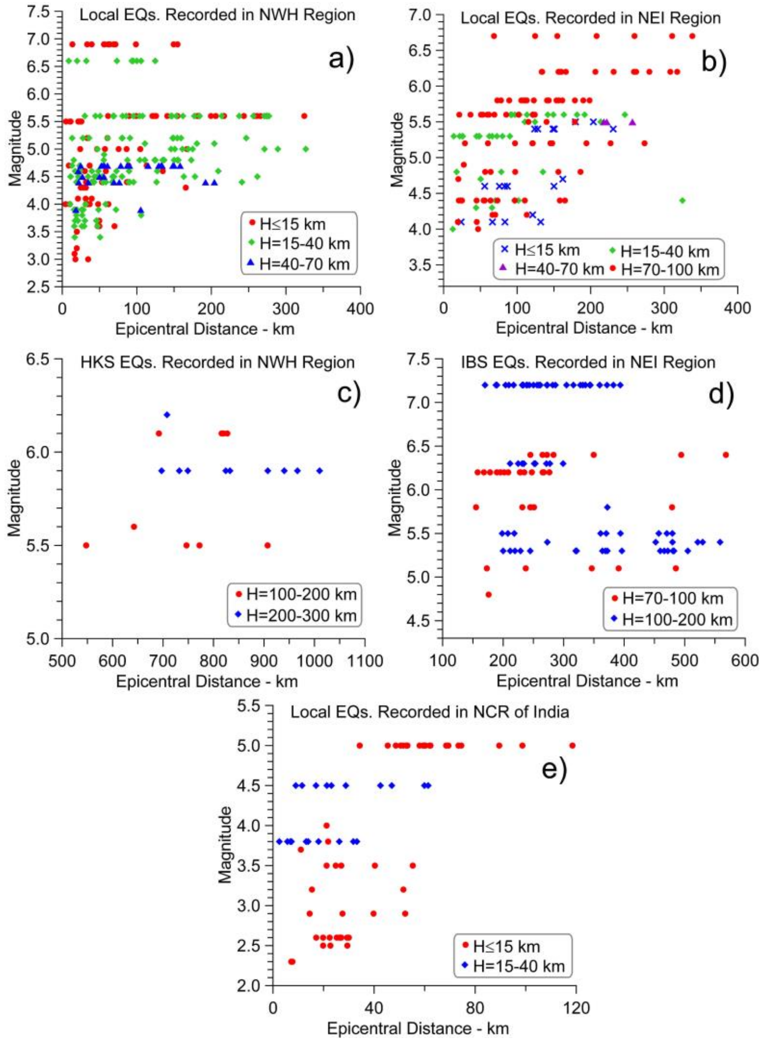

Fig. 2 The distributions of available strong motion records with respect to epicentral distance, earthquake magnitude, and focal depth in each of the five regions considered in this paper

Table 1: The Number of Records and Corresponding Ranges of Magnitude, Distance, and Depth of Available Data in Each Region

Region	No. of Records	Magnitude Range	Distance Range (km)	Depth Range (km)
NWH	249	3.0 – 6.9	4.4 – 326.6	5.0 – 52.5
NEI	149	4.0 – 6.7	12.5 – 337.9	7.0 – 79.0
HKS	19	5.5 – 6.2	547.7 – 1010.1	160.0 – 215.4
IBS	108	4.8 – 7.2	155.2 – 560.0	83.4 – 118.9
NCR	68	2.3 – 5.0	2.5 – 118.5	5.0 – 20.3

The number of three-component records used and the ranges of magnitude, epicentral distance, and focal depth covered by available data in each region are summarized in Table 1. The available number of records are seen to vary widely among the five regions, with the largest number of 249 records in the NWH region, and the smallest number of only 19 records in the HKS region. The available data is not sufficient to develop the prediction equation for the peak parameters of ground motion for any of the regions independently. A specially devised technique used by the authors (Gupta and Trifunac, 2017; 2018 a, b, c; 2019) to develop the empirical scaling equations for the Fourier and pseudo-relative velocity spectrum amplitudes for the same five regions is used in the present study and summarized in the next section of the paper.

The available database comprises a total of 593 three-component records (including 146 analog type records) giving a total of 593×3 = 1779 components of motion. These accelerograms have been suitably processed to minimize the low- and high-frequency noise and to correct for the baseline distortions as detailed in Gupta (2018). The analog records have been also processed to apply the instrument correction (Trifunac, 1972a; Chandrasekaran and Das, 1993). As the baseline correction involves high-pass filtering above a lower cut-off frequency specific to each component of motion (Gupta 2018), the peak amplitudes of ground displacement ($d_{\max}$) become lower than their true values. This has been compensated for by using random vibration theory in conjunction with the long-period extension of the empirically derived Fourier amplitude spectrum, FS, up to a 100 s period beyond the cut-off period, T_c, corresponding to the cut-off frequency used for baseline correction (Lee et al. 1995). The scaling factors for correction of the peak displacement amplitudes are then defined as the ratios of the integrals of the squares of the extended and the original Fourier Spectra. The distribution of the scaling factors obtained for all 1,779 components of ground motion is shown in the histogram of Figure 3. The $d_{\max}$ amplitudes thus corrected are used along with the peak acceleration amplitudes ($a_{\max}$) and peak velocity amplitudes ($v_{\max}$) to develop the empirical prediction relationships for all three peak parameters in all five zones considered in the present study.

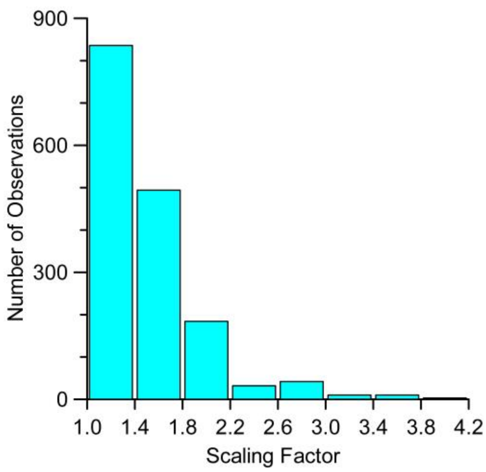

Fig. 3 A histogram of the correction factors for $d_{\max}$ amplitudes

PREDICTION MODEL AND REGRESSION ANALYSIS

1 Functional form of the Prediction Model

The functional form of the ground motion scaling and attenuation model used to develop the prediction relations for peaks of earthquake ground motion in this paper is the same as that used for developing the scaling model for Fourier spectrum amplitudes for the regions of Western Himalaya and Northeast India by Gupta and Trifunac (2017). This model can be expressed as

$$\begin{aligned}\log_{10} y = M + A_0 \log_{10} \Delta + C_1 + C_2 M + C_3 M^2 + \\ + C_4 v + C_5 s + C_6^0 S_L^0 + C_6^1 S_L^1 + C_6^2 S_L^2\end{aligned} \tag{1}$$

In this expression, y represents the $a_{\max}$, $v_{\max}$, or $d_{\max}$ amplitude, M denotes the earthquake magnitude, s denotes the site geology parameter (with s = 0 for alluvium, s = 1 for intermediate sites and s = 2 for basement rocks; as defined in Trifunac and Brady 1975), v denotes the component orientation (with v = 0 for horizontal and 1 for vertical component of motion), and S_L^0, S_L^1, and S_L^2 are indicator variables taking on the value of 1 for the site soil parameter s_L = 0, 1, and 2 representing rock soil, stiff soil, and deep soil, respectively, and zero otherwise. The coefficients C_1, C_2, C_3, C_4, C_5, C_6^0, C_6^1, and C_6^2 are the coefficients estimated by regression analysis of the recorded data.

The attenuation term, $A_0 \log_{10} \Delta$, is defined in terms of the representative distance Δ from the earthquake source to the site under consideration as proposed by Gusev (1983):

$$\Delta = S\left(\ln \frac{R^2 + H^2 + S^2}{R^2 + H^2 + S_0^2}\right)^{-\frac{1}{2}} \tag{2}$$

where R is the epicentral distance, H is the focal depth, S is the (magnitude-dependent) source size, and S_0 is the correlation radius of the source function.

The source size S (in km) is approximated empirically to be a linear function of earthquake magnitude M and is defined by (Gupta and Trifunac, 2017) as

$$S = \begin{cases} 0.2 \quad \text{for } M \le 3.0 \\ 0.2 + (S_{6.5} - 0.2)(M-3)/3.5 \quad \text{for } 3.0 < M \le 6.0 \\ 13.96 \quad \text{for } M > 6.0 \end{cases} \tag{3}$$

Here, $S_{6.5}$ is the fault rupture length for M = 6.5, which is obtained as 16.25 km from the following relationship for fault rupture length *L*(*M*) and rupture width *W*(*M*) as a function of earthquake magnitude *M*:

$$\begin{aligned} L(M) &= 0.0032 \times 10^{0.57M} \\ W(M) &= 0.0278 \times 10^{0.41M} \text{ for } M \ge 6 \\ W(m) &= L(m) \text{ for } M < 6. \end{aligned} \tag{4}$$

For magnitudes greater than 6.0, the source size is assumed not to increase and is assigned a maximum value of 13.96 km (equal to that for magnitude 6.0).

The correlation radius S_0 is defined by (Gusev, 1983) as

$$S_0 = \min\left(\frac{\beta T}{2}, \frac{S}{2}\right) \tag{5}$$

where β is the shear wave velocity at the earthquake source, taken equal to 3.5 km/s in the present study. Value of wave period T is taken as 0.1 s or 1.0 s for peak acceleration or peak velocity amplitudes, respectively. The correlation radius S_0 for the peak displacement is given as (Lee et al., 1995)

$$S_0 = \min\left(S_f, S\right)/2 \tag{6}$$

with

$$S_f = \begin{cases} L(M) \ \text{ for } M < 3.5 \\ \dfrac{L(M)}{2.2} + \dfrac{W(M)}{6.0} \ \text{ for } 3.5 \le M \le 7.0 \\ \dfrac{L(M_{\max})}{2.2} + \dfrac{W(M_{\max})}{6.0} \ \text{ for } M > M_{\max} = 7.0 \end{cases} \tag{7}$$

Further, very close to the source (say, hypocentral distance of less than 5 km) and for M<4.5, the representative distance Δ for the case of peak displacement can be approximated by

$$\Delta = S\left(\ln\left(\frac{S}{S_0}\right)^2\right)^{-1/2} \tag{8}$$

with the source size defined such that it is equal to the value of S for M = 4.5 with the magnitude dependence as per the empirical relationship, we obtain

$$S = 0.0193(5.5 - M)\times 10^{0.57M} \tag{9}$$

2. Common Regression Analysis for the NWH and NEI Regions

As previously mentioned, due to the limited strong motion data available, it is not possible to carry out a regression analysis on the model of Equation (1) for each region independently. The dependence on magnitude *M*, component of motion parameter v, site geological parameter s, and the site-soil condition parameter s_L is therefore estimated by a common regression analysis for the NWH and the NEI regions, which, with 249 and 149 three-component records, comprise the largest number, with a total of 398 records. A multistage regression analysis is used for this purpose, wherein a limited number of regression coefficients are estimated and constrained at each stage.

Stage-1: A combined equation of the following form is fitted for each of the three peak parameters in both the NEI and the NWH regions:

$$\begin{aligned} \log_{10} y - M = {} & A_0^E[(\log_{10}\Delta)\delta_E] + A_0^W[(\log_{10}\Delta)\delta_W] + \\ & C_4 v + C_5 s + \sum_{j=1}^{N} B_j e_j \end{aligned} \tag{10}$$

In this equation, δ_W and δ_E are the indicator variables with assigned values of 1.0 for the data points belonging to Northeast India and Western Himalaya, respectively, and 0.0 otherwise. The e_j is also an indicator variable assigned a value of 1.0 if the data belongs to the *j*-th of the N number of earthquakes and 0.0 otherwise. The use of independent regression coefficient B_j for each earthquake is able to account in a balanced way for the effect of different numbers of data points contributed by different earthquakes. The attenuation coefficients A_0^E and A_0^W for the NEI and NWH regions, respectively, and the common coefficients C_4, C_5 and B_j for *j* = 1 to *N* in Eq. (10) are estimated by a simple least-squares regression analysis using 1,194 components of ground motion data points corresponding to 398 three-component records for both the NEI and the NWH regions.

To minimize the possible bias that may arise due to an uneven distribution of data over different magnitudes, the data points actually used in the analysis, - i.e., site geology parameters, site soil condition parameters, and the components of motion - are obtained using a decimation scheme proposed by Trifunac and Anderson (1977). Also, the 28 data points with significantly small $a_{\max}$ below 1.0 cm/s^2, all of which belong to the NWH region, have been excluded being close to the noise level. The remaining 1166 data points for each of $a_{\max}$, $v_{\max}$, and $d_{\max}$ are separated into the magnitude groups of 3–3.9, 4–4.9, 5–5.9, and 6–6.9. The data points in each magnitude group are then successively subdivided according to site geology parameter s (= 0, 1 and 2), site soil parameter s_L (= 0, 1 and 2), and component orientation parameter v (= 0, 1), giving a total of 72 subgroups of data for each peak parameter. The data in each subgroup is arranged in increasing order of the peak-amplitude values and a maximum of only 33 data points closest to the 3rd, 6th,….., 96th, and 99th percentile positions are retained. By this procedure, the 1,166 data points are reduced to 788 data points for each of the peak parameters, which are then used in the Eq. (10) regression analysis.

Stage-2: In this stage of analysis, a two-step weighted regression analysis (Searle et al., 1971) is applied to estimate the regression coefficients defining the earthquake magnitude dependence common to both the NEI and NWH regions. In the first step, the following equation is fitted by a simple least-squares regression analysis:

$$\log_{10} y - M - A_0^E[(\log_{10}\Delta)\delta_E] - A_0^W[(\log_{10}\Delta)\delta_W] - C_4 v - C_5 s = \sum_{j=1}^{J} B_j e_j \tag{11}$$

The magnitude dependence is defined in the second step by a weighted least-squares regression analysis on the following system of equations:

$$B_j = C_1^E \delta_E + C_1^W \delta_W + C_2 M_j + C_3 M_j^2 \tag{12}$$

The weight for the jth earthquake contributing n_j number of data points is defined by $w_j = (\sigma_1^2 / n_j + \sigma_2^2)^{-1}$ with σ_1^2 and σ_2^2 as the variances of the fitting of Eqs. (11) and (12), respectively. As the variance σ_2^2 for the second step of regression analysis is not known in advance, an iterative search method is used by starting with an initial value of σ_2^2 as zero and increasing it in very small steps. The value of σ_2^2, which results in a weighted variance of the fitting of Eq. (12) close to 1.0, indicates the condition of convergence. To achieve negative values for the coefficient C_3 in Eq. (12) to meet the physical requirement of magnitude saturation, only 704 data points with magnitudes 4.0 or above have been used in this stage of analysis out of the 788 decimated data points used in the Stage-1 analysis.

Stage-3: The dependence on the site soil condition is next developed by a least-squares fitting of the following equation using all 788 decimated data points for both the NEI and NWH regions:

$$\begin{aligned} \log_{10} y - M - A_0^E[(\log_{10}\Delta)\delta_E] - A_0^W[(\log_{10}\Delta)\delta_W] - C_1^E\delta_E - C_1^W\delta_W - \\ C_2 M - C_3 M^2 - C_4 v - C_5 s = C_6^0 S_L^0 + C_6^1 S_L^1 + C_6^2 S_L^2 \end{aligned} \tag{13}$$

Table 2: Regression Coefficients Defining the Dependences on the Earthquake Magnitude, Component of Motion, Site Geological Condition and Site Soil Condition for Both NEI and NWH Regions

Parameter	a_{max} (cm/s^2)	v_{max} (cm/s)	d_{max} (cm)
C_2	-0.310832	-0.101431	0.117228
C_3	-0.018108	-0.025898	-0.018373
C_4	-0.167876	-0.279776	-0.259237
C_5	0.020532	-0.022429	-0.037847
C_6^0	0.038012	-0.007977	-0.046398
C_6^1	0.051841	0.051274	0.063319
C_6^2	0.068059	0.099612	0.123517

This completes the estimation of the regression coefficients C_2, C_3, C_4, C_5, C_6^0, C_6^1, and C_6^2 common to both the NWH and NEI regions, which will also be assumed to be applicable to the other three regions. The values of these coefficients defining the dependence on magnitude M, component of motion parameter v, site geology parameter s, and site soil condition parameter s_L for the peak parameters $a_{\max}$, $v_{\max}$ and $d_{\max}$ are listed in Table 2.

3. Prediction Models and Statistics of Residues for the NWH and NEI Regions

In the preceding analysis, the distance attenuation coefficients A_0^E and A_0^W and the corresponding constant terms C_1^E and C_1^W for the NEI and the NWH regions, respectively, have been estimated simultaneously using the combined data set for both the regions. Some degree of trade-off between the values of these coefficients for the two regions cannot thus be ruled out. The 788 decimated data points for both regions are therefore separated out into 526, 521, and 512 data points respectively for the $a_{\max}$, $v_{\max}$, and $d_{\max}$ amplitudes in the NWH region and into 262, 267, and 276 data points respectively for the $a_{\max}$, $v_{\max}$, and $d_{\max}$ amplitudes in the NEI region. The data points for the respective peak parameters and the region are used to estimate the final values of the attenuation coefficient A_0 and the constant coefficient C_1 by regression analysis on the following equation:

$$\log_{10} y - M - C_2 M - C_3 M^2 - C_4 v - \mathrm{C}_5 s - C_6^0 S_L^0 - C_6^1 S_L^1 - C_6^2 S_L^2 = A_0 \log_{10} \Delta + C_1 \tag{14}$$

The values of A_0 and C_1 thus obtained independently for the NWH and NEI regions are given in Tables 3 and 4, respectively.

Table 3: Attenuation Coefficient A_0, Constant Term C_1, and the Statistical Parameters for the Gaussian Distribution of the Residuals for the Three Peak Amplitudes for the Local Earthquakes Recorded in the NWH Region

Parameter	$a_{\max}$ (cm/s^2)	$v_{\max}$ (cm/s)	$d_{\max}$ (cm)
A_0	-1.106289	-1.035888	-1.123484
C_1	-0.003742	-2.373145	-4.559549
μ	0.0	0.0	0.0
σ	0.32800	0.34744	0.37094
KS	0.036	0.030	.026
$KS_{0.95}$	.059	.060	.060
χ^2	10.05	7.14	9.90
$\chi^2_{0.95}$	14.07	14.07	14.07

Table 4: Attenuation Coefficient A_0, Constant Term C_1, and the Statistical Parameters for the Gaussian Distribution of the Residuals for the Three Peak Amplitudes for the Local Earthquakes Recorded in the NEI Region

Parameter	$a_{\max}$ (cm/s^2)	$v_{\max}$ (cm/s)	$d_{\max}$ (cm)
A_0	-1.310963	-1.241734	-1.091398
C_1	0.762275	-1.660238	-4.304131
μ	0.0	0.0	0.0
σ	0.27786	0.29786	0.32542
KS	0.062	0.042	0.032
$KS_{0.95}$	0.084	0.083	0.082
χ^2	10.94	5.19	9.81
$\chi^2_{0.95}$	14.07	14.07	14.07

The coefficients A_0 and C_1 given in Tables 3 and 4, along with the common regression coefficients given in Table 2, can be used to estimate expected value $\hat{y}$ of the three peak parameters in the NWH and NEI regions, respectively, from the prediction model of Eq. (1) as follows:

$$\log_{10}\hat{y} = M + A_0\log_{10}\Delta + C_1 + C_2M + C_3M^2 + C_4v + C_5s + C_6^0S_L^0 + C_6^1S_L^1 + C_6^2S_L^2 \qquad (15)$$

For given values of variables M, Δ, v, s, and s_L, Eq. (15) has a parabolic dependence on magnitude M. As in Gupta and Trifunac (2017), it is thus assumed that this equation applies only in the range of $M_{\min} \le M \le M_{\max}$ with

$$M_{\min} = -C_2/(2C_3) \qquad \text{and} \qquad M_{\max} = -(1+C_2)/(2C_3) \qquad (16)$$

For magnitudes below $M_{\min}$, M in the terms $C_1M + C_2M^2$ is replaced by $M_{\min}$, whereas for magnitudes greater than $M_{\max}$, M is replaced by $M_{\max}$ throughout Equation (15).

The differences between the logarithm of the recorded values y of a peak parameter ($a_{\max}$, $v_{\max}$ or $d_{\max}$) and the corresponding expected values $\log_{10}\hat{y}$ obtained from the prediction relationship of Equation (15) gives the residues $\in$ as

$$\in = \log_{10} y - \log_{10}\hat{y} \qquad (17)$$

Following Gupta and Trifunac (2017), it is assumed that the residues of the recorded data for all three peak amplitudes can be described by a normal distribution function with the mean value μ and the standard deviation σ of the residues. The values of statistical parameters μ and σ obtained for the three peak parameters are also given in Tables 3 and 4 for the NWH and NEI regions, respectively. These can be used to define the probability of having the value of the residues less than or equal to a specified value $\in$ as:

$$p(\in) = \frac{1}{\sigma\sqrt{2\pi}}\int_{-\infty}^{\in}\exp\left[\frac{-1}{2}\left(\frac{x-\mu}{\sigma}\right)^2\right]dx \qquad (18)$$

To test the null hypothesis H_0 that the Gaussian probability distribution can be used to describe the statistics of the residuals, the Kolmogorov–Smirnov (KS) and chi-square (χ^2) statistical tests are performed as in Trifunac (1987). For this purpose, the KS and χ^2 estimates along with their respective 95% cutoff levels $KS_{0.95}$ and $\chi_{0.95}$ for rejecting the hypothesis are also listed for NWH and NEI regions in Tables 3 and 4, respectively. At the 95% confidence, both the KS and the χ^2 tests are not seen to reject the assumption that the Gaussian distribution can describe the distribution of residues for all three peak parameters.

4. Prediction Models for the NCR, IBS, and HKS Regions

A perturbation method is used to develop the prediction relations for the three peak parameters of earthquake ground motion in the National Capital Region (NCR) of India, the Indo-Burmese subduction (IBS) earthquakes recorded in NEI region, and the Hindu Kush subduction (HKS) earthquakes recorded in the NWH region, all of which have a limited number of strong motion records. In this approach, the dependence on magnitude M, component of motion parameter v, site geological parameter s, and site-soil condition parameter s_L is taken the same as that obtained for the NWH and the NEI regions with a much larger database, which is defined by the regression coefficients given in Table 2. To define the complete prediction relationships, the distance attenuation and the constant terms are only evaluated by the regression analysis in Equation (14) of the limited database available for these three regions. The prediction relationships thus developed are then used to analyse the statistics of residuals using the same database.

There are a total of 204 data points from 68 three-component records from the local earthquakes recorded in the NCR of India. After excluding 5 data points with $a_{\max}$ below 1.0 cm/s^2, the remaining 199 data points are used in the present analysis. No further reduction has occurred in these data points due to the process of decimation used to minimize the possible bias due to the uneven distribution of data over different magnitudes, site geology parameters, site-soil condition parameters, and components of motion. The decimation was attempted by retaining a maximum of 16 data points closest to the 6^{th}, 12^{th},….., 90^{th}, and 96th percentile positions for each data group as defined in the case of the NWH and NEI regions. The regression coefficients and the statistical parameters for the three peak parameters obtained using the 199 data points for the NCR of India are listed in Table 5. The assumption that the Gaussian distribution can describe the distribution of the residuals of all three peak parameters of ground motion in the NCR is not rejected by the KS as well as the χ^2 tests at the 95% confidence.

Table 5: Regression Coefficients and Statistical Parameters for the Gaussian Distribution of the Residuals for the Three Peak Amplitudes for the Local Earthquakes Recorded in the NCR

Parameter	a_{max} (cm/s^2)	v_{max} (cm/s)	d_{max} (cm)
A_0	-1.649400	-1.594599	-1.517270
C_1	1.035711	-1.434263	-4.034816
μ	0.0	0.0	0.0
σ	0.33732	0.36485	0.38809
KS	0.062	0.048	0.054
$KS_{0.95}$	.0964	.0964	.0964
χ^2	11.10	11.76	7.26
$\chi^2_{0.95}$	14.07	14.07	14.07

For the IBS earthquakes recorded in the NEI region, we have a total of 324 data points from 108 three-component strong motion records. All these records are characterized by a_{max} values greater than or equal to 1.0 cm/s^2. To estimate the regression coefficient A_0 and C_1 from Eq. (14) and to analyze the statistics of the residuals, a reduced database of 224 data points obtained by retaining a maximum of 19 data points closest to the 5th, 10^{th},….., 90^{th}, and 95th percentile positions for each data group is used. The regression coefficients and statistical parameters thus obtained are listed in Table 6. The validity of the Gaussian distribution for all three peak parameters recorded in the NEI region from the IBS earthquakes is established by the KS test and as well as the χ^2 test for the residues of v_{max} and d_{max}. The χ^2 test is seen to reject the Gaussian hypothesis only marginally for the case of a_{max}.

Table 6: Regression Coefficients and Statistical Parameters for the Gaussian Distribution of the Residuals for the Three peak Amplitudes for the IBS Earthquakes Recorded in the NEI region

Parameter	a_{max} (cm/s^2)	v_{max} (cm/s)	d_{max} (cm)
A_0	-1.061131	-.950267	-1.432349
C_1	0.416568	-2.218496	-3.493796
μ	0.0	0.0	0.0
σ	0.26197	0.27431	0.29743
KS	0.042	0.053	0.035
$KS_{0.95}$	0.091	0.091	0.091
χ^2	14.91	12.63	4.68
$\chi^2_{0.95}$	14.07	14.07	14.07

A very meagre database of only 57 data points from 19 three-component records is available for the HKS earthquakes recorded in the NWH region. Only 49 data points with $a_{\max}$ values greater than or equal to 1.0 cm/s^2 are used in the present study. This has been further reduced marginally to 47 data points by retaining a maximum of 9 data points closest to the 10th, 20th,….., 80th, and 90th percentile positions for each data group. These 47 data points are used to estimate the regression coefficient A_0 and C_1 from Eq. (14) and to analyze the statistics of the residuals, and the results obtained are given in Table 7. Although the KS test does not reject the applicability of the Gaussian distribution to all three peak parameters, the χ^2 test at a 95% confidence level rejects the Gaussian hypothesis for the residuals of $a_{\max}$ and $v_{\max}$ amplitudes, which may be related to the very small sample size of only 47 data points. However, the Gaussian distribution may still be used with the belief that it will not be rejected when more of the recorded data becomes available.

Table 7: Regression Coefficients and Statistical parameters for the Gaussian Distribution of the Residuals for the Three Peak Amplitudes for the HKS earthquakes Recorded in the NWH region

Parameter	a_{max} (cm/s^2)	v_{max} (cm/s)	d_{max} (cm)
A_0	-0.607183	-0.831728	-1.019233
C_1	-1.297295	-2.765896	-4.573787
μ	0.0	0.0	0.0
σ	0.18056	0.25485	0.34344
KS	0.106	0.112	0.071
$KS_{0.95}$	0.198	0.198	0.198
χ^2	17.92	22.82	8.78
$\chi^2_{0.95}$	14.07	14.07	14.07

COMPARISONS OF RECORDED AND PREDICTED PEAK AMPLITUDES

We now show that the prediction relations developed for the three peak parameters ($a_{\max}$, $v_{\max}$ and $d_{\max}$) in the five different regions encompassing the Himalayan orogenic belt can provide the empirical estimates in good agreement with the available recorded data. For this purpose, a set of six plots is presented for each region with two plots for each of the three peak parameters as given in Figures 4 to 8 for the NWH, NEI, NCR, IBS and HKS regions, respectively. The first plot (left-hand side panels in Figures 4 to 8) for each peak parameter in a region shows the predicted vs. observed peak amplitudes along with the continuous 1:1 line idealizing the exact matching and two dashed lines representing an 80% confidence interval between the 10% and 90% confidence levels. This has been termed as the scatter plot. The second plot (right-hand side panels in Figures 4 to 8), termed as the attenuation plot, shows the normalized observed data vs. the hypocentral distance, where normalization is carried out to a specified magnitude, horizontal component of motion ($v = 0$), basement rock type of site geology ($s = 2$), and hard rock type of site soil condition ($s_L = 0$). These plots also show the attenuation curves computed from the developed prediction relationships for confidence levels of p = 0.1, 0.5, and 0.9 for the parameters used for normalization of observed data, where the attenuation curves for p = 0.1 and 0.9 represent the 80% confidence interval.

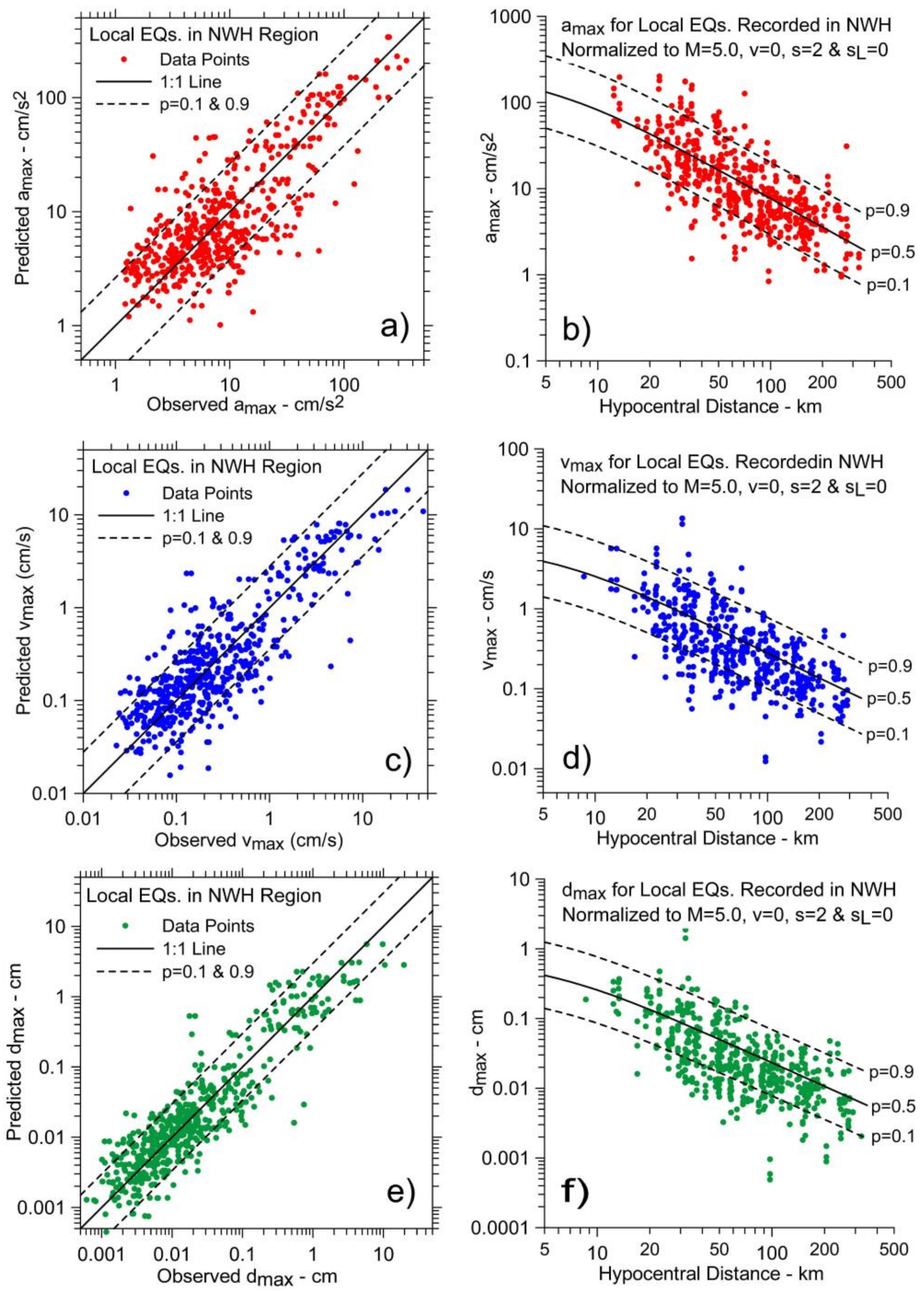

Fig. 4 Comparisons of the predicted vs. observed peak amplitudes (left-hand panels) and the observed peak amplitudes normalized to M = 5.0 as a function of the hypocentral distance with the mean and 80% confidence intervals (right-hand panels), and the top, middle, and bottom panels corresponding to $a_{\max}$, $v_{\max}$, and $d_{\max}$, respectively, for the local earthquakes recorded in the NWH region

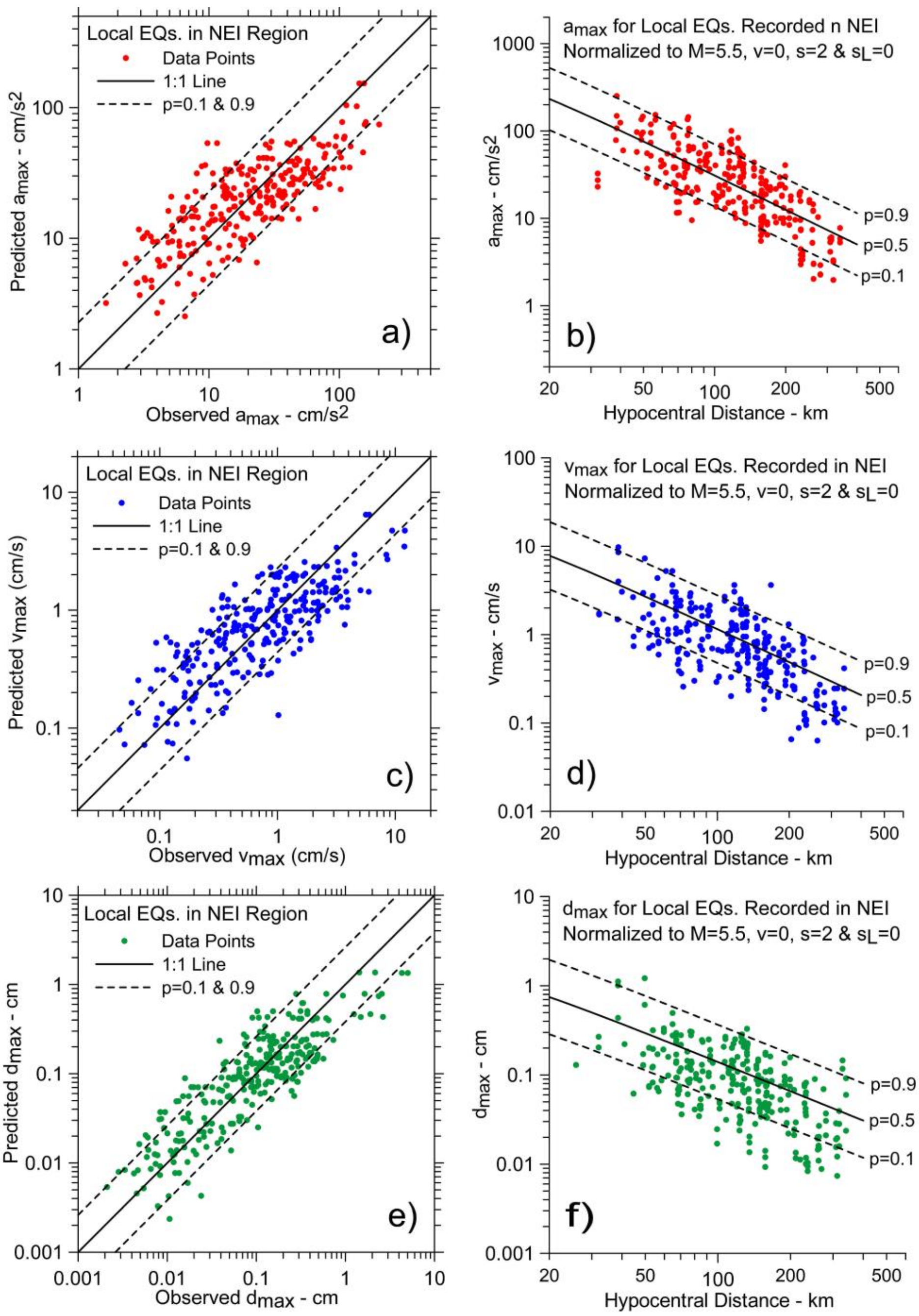

Fig. 5 Comparisons of the predicted vs. observed peak amplitudes (left-hand panels) and the plots of observed peak amplitudes normalized to M = 5.5 as a function of the hypocentral distance with the mean and 80% confidence intervals (right hand panels), and the top, middle and bottom panels corresponding to $a_{\max}$, $v_{\max}$ and $d_{\max}$, respectively, for the local earthquakes recorded in the NEI region

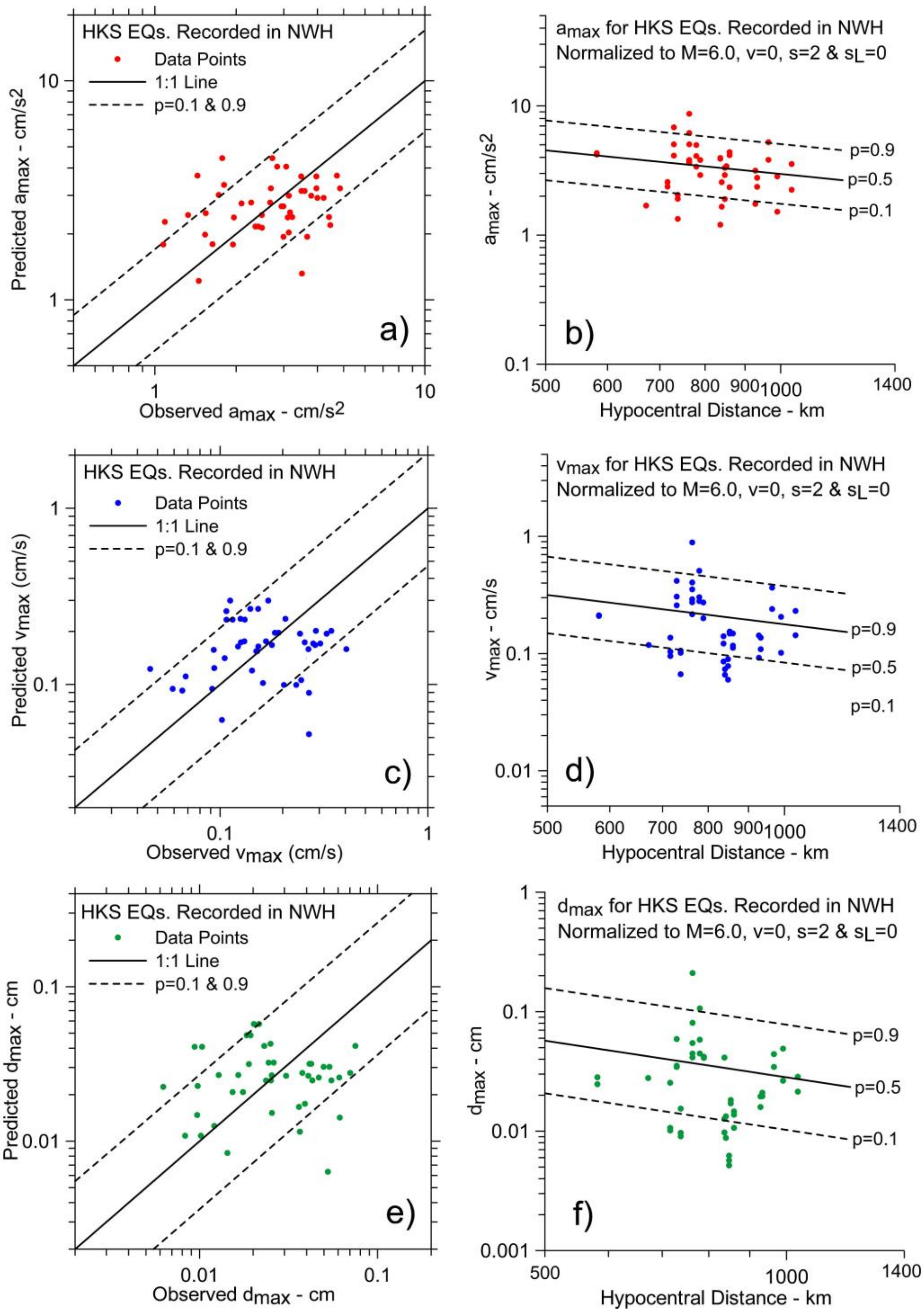

Fig. 6 Comparisons of the predicted vs. observed peak amplitudes (left-hand panels) and the plots of observed peak amplitudes normalized to M = 6.0 as a function of the hypocentral distance with the mean and 80% confidence intervals (right hand panels), and the top, middle and bottom panels corresponding to $a_{\max}$, $v_{\max}$ and $d_{\max}$, respectively, for the local earthquakes recorded in the HKS region

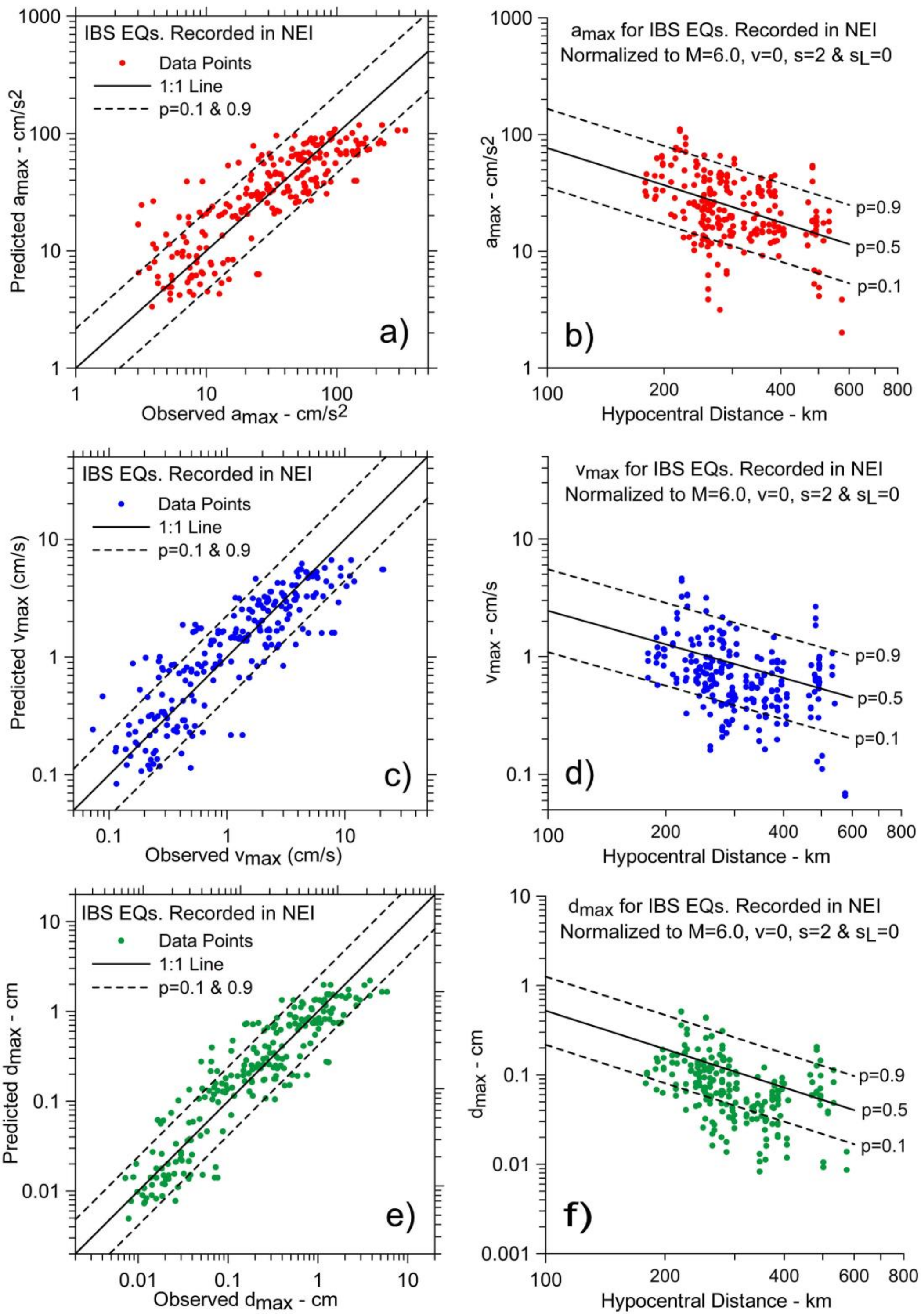

Fig. 7 Comparisons of the predicted vs. observed peak amplitudes (left-hand panels) and the plots of observed peak amplitudes normalized to M=6.0 as a function of the hypocentral distance with the mean and 80% confidence intervals (right hand panels), and the top, middle and bottom panels corresponding to a_{max}, v_{max} and d_{max}, respectively, for the local earthquakes recorded in the IBS region

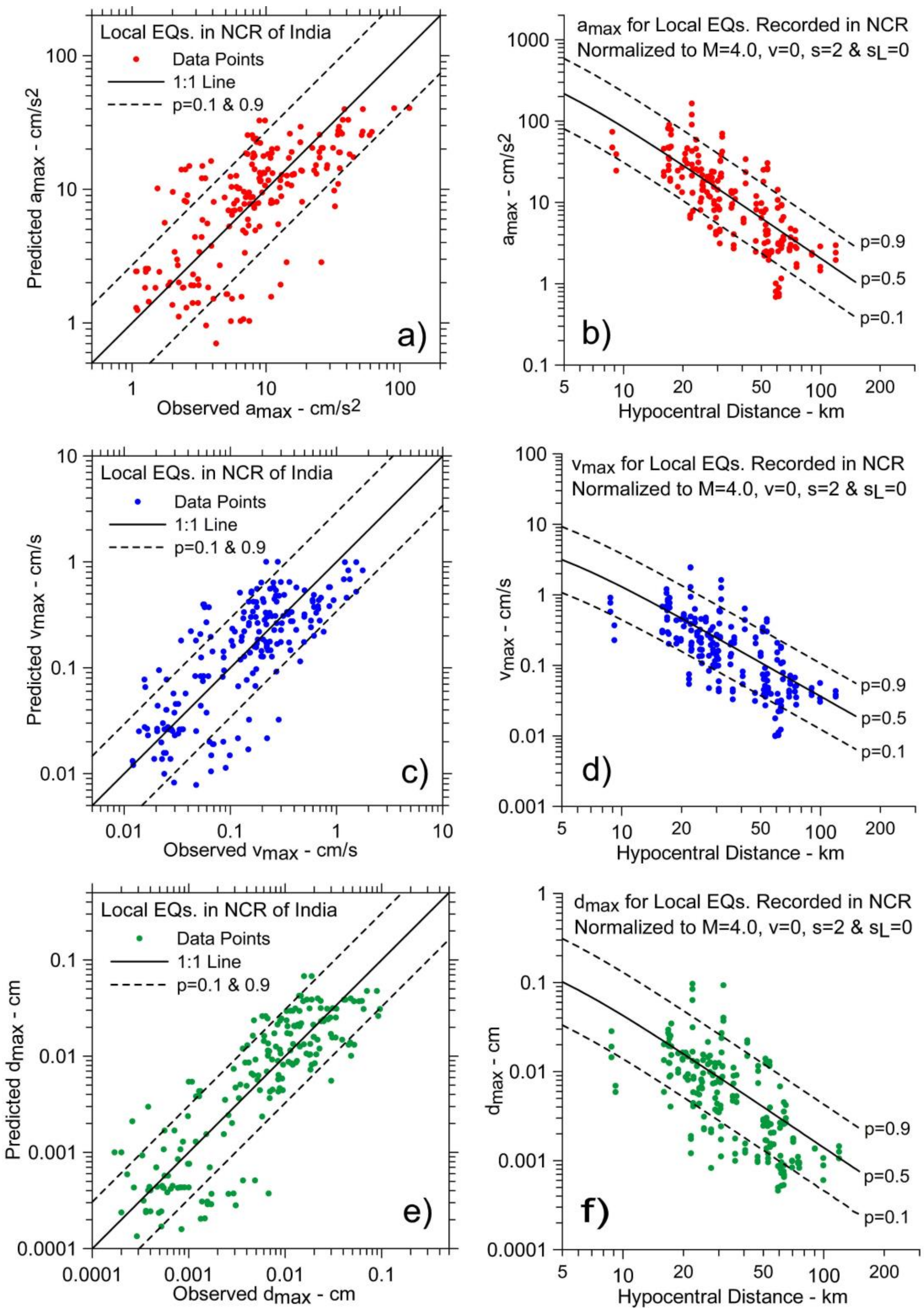

Fig. 8 Comparisons of the predicted vs. observed peak amplitudes (left-hand panels) and the plots of observed peak amplitudes normalized to M = 4.0 as a function of the hypocentral distance with the mean and 80% confidence intervals (right hand panels), and the top, middle and bottom panels corresponding to $a_{\max}$, $v_{\max}$ and $d_{\max}$, respectively, for the local earthquakes recorded in the NCR region

The scatter and attenuation plots in Figures 4 to 8 are used to assess the quality of agreement between the observed data and the estimates from the developed prediction relations by finding the fraction of the observed data points lying within the p = 0.1–0.9 confidence interval, which is required to be 80% or more for excellent agreement. The estimates of these percentages for all five regions and three peak parameters for each region are summarized in Table 8. The first four columns from left to right in this table give the serial number of the region, the abbreviation used to identify the region, the type of peak parameter, and the total number of data points used in the regression analysis. The last two columns give the total number and percentage of data points lying within p = 0.1–0.9 band, which are the same for the scatter as well as the attenuation plots.

The results in Table 8 indicate that in 11 out of the total of 15 cases (5 regions × 3 peak parameters), the fraction of data points within the p = 0.1–0.9 confidence interval is higher than or equal to 79.9%. This can be taken to represent very good matching between the observed and predicted peak amplitudes. Moreover, in the remaining four cases, this fraction is higher than 77%, which can also be considered to represent good matching. The largest number of data points in all 15 cases are seen to be clustered close to the 1:1 line in the scatter plots and the median curve in the attenuation plots. Thus, the empirical prediction relations developed in this study can be considered to describe the observed data well.

Table 8: Percentage of Observed Data Lying Within p = 0.1–0.9 Confidence Intervals in the Scatter Plots given in the left-hand side panels and attenuation plots given on the right-hand side of Figures 4 to 8 for the Peak Amplitudes Recorded in the Five Regions

Sr. No	Region	Peak Parameter	Total No. of Data	Data within p=0.1–0.9	% of Data
1.	NWH	a_{max}	526	427	81.2
		v_{max}	521	423	81.2
		d_{max}	512	415	81.2
2.	NEI	a_{max}	262	206	78.6
		v_{max}	267	207	77.5
		d_{max}	276	213	77.2
3	NCR	a_{max}	199	162	81.4
		v_{max}	199	159	79.9
		d_{max}	199	159	79.9
4	IBS	a_{max}	224	185	82.6
		v_{max}	224	180	80.4
		d_{max}	224	179	79.9
5	HKS	a_{max}	47	37	78.7
		v_{max}	47	38	80.9
		d_{max}	47	39	82.9

VALIDATION AT EARTHQUAKE SOURCE

In the previous section, the validity of the prediction relations developed in this paper has been addressed by showing the degree of matching of the observed and the estimated amplitudes of the three peak parameters. In this section we examine other validations based on the seismological estimates of stress drop in India and for a comparison in California.

Figure 9 shows a qualitative comparison of the maximum displacement at faults (hypocentral distance of zero) for different magnitudes as obtained from the prediction equations developed for the NWH, NEI, NCR, HKS and IBS regions, with such trends reported by Thatcher and Hanks (1973) and Trifunac (1972 b, c) for California earthquakes. It is seen that while our equations extrapolated to zero epicentral distances are in fair agreement with observed trends for intermediate and small earthquakes, our equations lead to a smaller rate of growth of fault displacement vs. magnitude for larger earthquake events. The observed differences are caused by regional differences between the Himalayan and California seismogenic zones, specifically in terms of their depths and geometries. Also, there are differences between the somewhat gently dipping, thrust-type faulting mechanism of Himalayan earthquakes compared to steeply dipping and strike-slip faulting of California earthquakes.

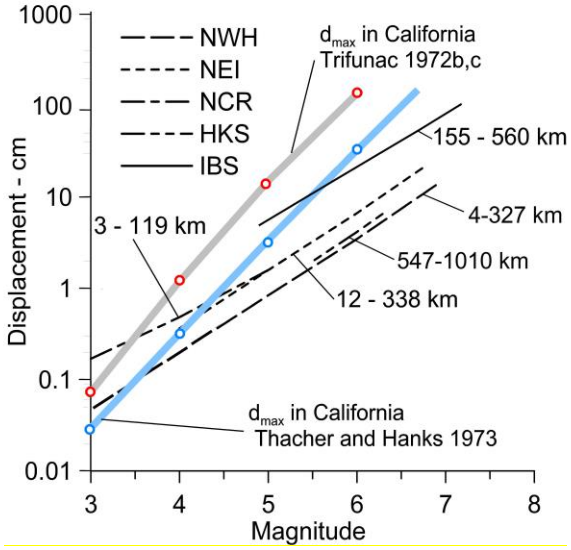

Fig. 9 Extrapolated peak displacements to zero hypocentral distance and a comparison with such trends in California (Trifunac 1972 b, c; Thacher and Hanks 1973). Peak displacement amplitudes are plotted only within the magnitude ranges for which the data is available. The numbers at each line show the distance range for which strong motion data was available for the regressions presented in this paper (e.g., 3 to 119 km for events in the NCR region)

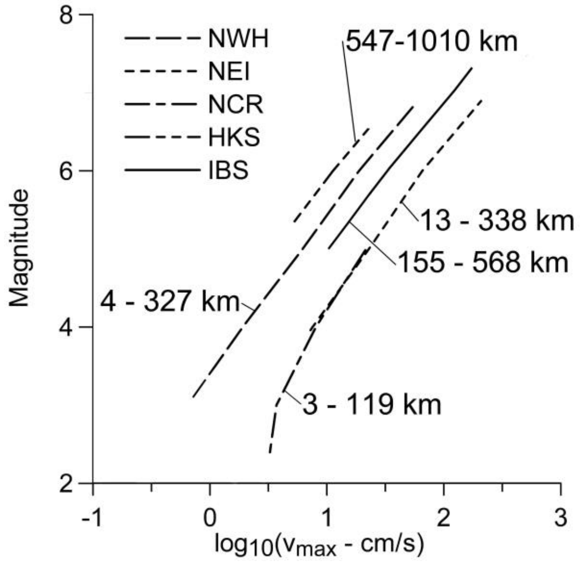

Fig. 10 Extrapolated peak velocities to zero hypocentral distance for the NWH, NEI, NCR, HKS and IBS regions. Predicted peak velocities are plotted only within the magnitude ranges for which corresponding data is available. The numbers at each line show the distance range for which strong motion data was available for the regressions presented in this paper (e.g., 3 to 119 km for events in the NCR region)

Figure 10 shows the same rate of increase in peak velocities vs. magnitude in all regions studied in this paper and the largest peaks associated with large events in the IBS, NEI and NWH regions. As in Figure 9, the trends are shown only within the magnitude intervals for which strong motion data is available.

Figures 11 and 12 compare the magnitude dependence of peak strong motion velocities via their rough estimates in terms of stress drop at the earthquake faults. Because no measurements of strong motion velocities exist at the earthquake sources, we perform rough comparison of velocities via reported values of stress drop. For this purpose, we employ the far-field body wave spectra of shear waves and

Brune's model (Trifunac 1972b,c) that describes the first-order relationship between the ground velocity v and stress drop σ as in $v \sim \sigma\beta / \mu$, where β is the shear wave velocity in the source region and μ is the shear modulus of the surrounding rocks. We assume that peak velocity $v_{\max}$ is also proportional to $\sigma\beta / \mu$ and compute σ from $\sigma \sim v_{\max}\mu / \beta$. However, the $v_{\max}$ amplitudes of the empirical scaling relations are diminished due to anelastic attenuation, which can be approximated by $\exp[-(\pi f \Delta)/(\beta Q(f))]$, where β is the average shear wave velocity along the source-to-site travel path. The peak velocity from the empirical scaling relations corrected for anelastic attenuation thus leads to the following approximation for the stress drop:

$$\sigma_{eff} \cong \mu_{source} v_{\max} e^{\pi f \Delta_0 / \beta Q} / \beta_{source} \tag{19}$$

where σ_{eff} is the Brune effective stress taken to be representative of the stress drop parameter as we use it in this paper (Trifunac 1972b). The expression of Equation (19) is used to estimate the values of stress drop for different magnitudes in the five different regions considered in the present study assuming that $v_{\max}$ is associated with frequencies in the vicinity of 1.0 Hz. The β_{source} and μ_{source} used for this purpose are the same as given in our earlier work on scaling equations for Fourier and response spectral amplitudes for the same regions (Gupta and Trifunac 2017, 2018a,b,c, 2019). These are $\beta_{source} = 3.3$ km/s and $\mu_{source} = 3.0 \times 10^{11}$ dyne/cm^2 for the NWH region, $\beta_{source} = 3.5$ km/s and $\mu_{source} = 3.4 \times 10^{11}$ dyne/cm^2 for both the NEI region and the NCR of India, $\beta_{source} = 4.2$ km/s and $\mu_{source} = 5.9 \times 10^{11}$ dyne/cm^2 for IBS earthquakes recorded in the NEI region, and $\beta_{source} = 4.9$ km/s and $\mu_{source} = 7.56 \times 10^{11}$ dyne/cm^2 for HKS earthquakes recorded in the NWH region. To evaluate the correction factor $f_0 = \exp[(\pi f \Delta_0)/(\beta Q(f))]$ for anelastic attenuation along the travel path, we also need to specify average distance Δ_0 at which the available database has been recorded, shear wave velocity β along the travel path between the source and recording station, and frequency-dependent quality factor $Q(f)$ for each combination of earthquake and the region of observation. The values of these parameters used and the correction factors f_0 obtained for all the five regions are summarized in Table 9.

Table 9: The Average Distance of Recording Δ_0, Q-factor at $f = 1.0$ Hz, and Shear Wave Velocity β Along the Travel Path Used to Obtain the Correction Factors f_0 for Anelastic Attenuation for the Five Regions Considered in this Study

Region	Distance Δ_0 (km)	$Q(f = 1.0$ Hz$)$	Wave velocity β (km/s)	Correction factor f_0
NWH	125	70	3.3	5.47
NEI	200	200	3.5	2.45
NCR	50	150	3.0	1.42
IBS	400	400	4.54	2.00
HKS	800	70 for Δ≤100 km 750 for Δ>100 km	3.3 for Δ≤100 km 5.0 for Δ>100 km	7.00

In Table 9, the average distances of recording Δ_0 for various regions are decided subjectively from the plots in Figure 2. The values of the Q-factors have been decided judiciously from the published literature. A large number of publications have developed frequency-dependent relations for the anelastic attenuation factor $Q(f)$ for different parts of the NWH region (e.g., Nath et al., 2008a; Joshi et al., 2010 2012; Harbindu et al., 2012; Chopra et al., 2012; Sharma et al., 2014; Vandana et al., 2015; Kumar et al., 2015). The value of 70 adopted in Table 9 is the median of the 11 values from these publications, which vary widely between 28 and 159 at 1.0 Hz. For the NEI and IBS regions, Raghukanth and Somala (2009) obtained the relations $Q(f) = 224 f^{0.93}$ and $Q(f) = 431 f^{0.70}$, respectively, which have been used to assign the Q-values for these zones in Table 9. The value for the NCR of India has been decided from the relation $Q(f)=142 f^{1.04}$ developed by Mohanty et al. (2009). Finally, for the HKS earthquakes at very long distances, the Q-factor up to 100 km taken is the same as that of the local earthquakes in the NWH region, and the value of 750 adopted for longer distances is based on Wu and Aki (1988).

The shear wave velocity β of 3.3 km/s and 3.0 km/s given in Table 9 for the crustal earthquakes in the NWH region and the NCR of India, respectively, are based on the trend of the values indicated by crustal models developed by Borah et al. (2015) using the receiver function method. The β value of 3.5 km/s for crustal earthquakes in the NEI is also based on receiver function modelling for the region developed by Borgohain and Bora (2018) and Saikia et al. (2016). The $\beta=4.54$ km/s for the IBS earthquakes at a very long distance is the average value obtained by assuming that the nearest 100 km of the wave path is traveled through the Earth's crust with $\beta=3.5$ km/s in the NEI and the remaining wave path is traveled through the upper mantle with $\beta=5.0$ km/s. For the HKS earthquakes, $\beta=3.3$ km/s for the nearest 100 km is the crustal velocity in the NWH region and $\beta=5.0$ km/s for longer distances corresponds to the wave path through the upper mantle. The correction factors obtained are given in the last column of Table 9.

The expression of Equation (19) is used to estimate the stress drop for different magnitudes in all five regions based on the β_{source} and μ_{source} values previously mentioned, the correction factor for anelastic attenuation as obtained in Table 9, and the predicted peak velocity amplitude $v_{\max}$ extrapolated to a zero hypocentral distance. In Figure 11, we compare our estimates of σ for the NWH and in Figure 12 for the NEI, with various published estimates of σ. In all calculations of σ, we also introduce a correction factor of 1.65 to compensate approximately for the decay of high-frequency spectral amplitudes beyond $f_{\max}$ (Gičev and Trifunac 2022). This correction was introduced in addition to the correction for anelastic attenuation with factors f_0 given in Table 9. We show a comparison of our results for σ with published stress-drop estimates only for the NWH and the NEI. There is not enough published data to make similar comparisons for sources in the NCR, HKS, and IBS based on earthquake recordings.

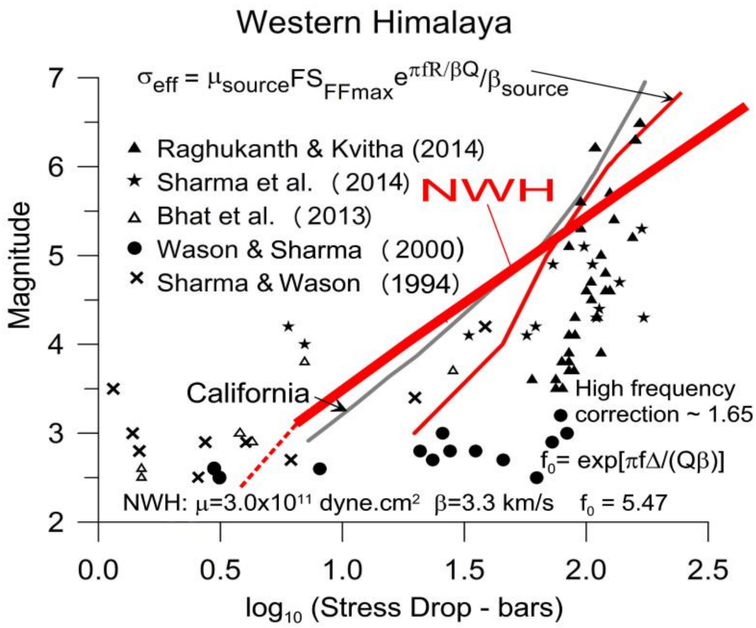

Fig. 11 A comparison of the stress drop trend vs. magnitude (wide red line for magnitudes between 3 and 7) based on $v_{\max} \sim \sigma\beta/\mu$ with the peak velocities for different magnitudes at the fault surface estimated for the NWH in this paper by extrapolation of regressed attenuation equation for $v_{\max}$, with (a) independent estimates of published values of stress drop by different investigators, (b) with average trends in California, and (c) with estimates of σ_{eff} based on empirical scaling model for Fourier Spectra (FS) by Gupta and Trifunac (2017)

By the way of a general comparison with other source regions, having different stress conditions and different types of faulting, in Figure 13 we illustrate a comparison of the trends for σ based on strong motion data in India, vs. earthquake magnitude, with such corresponding estimates for stress drop based on strong motion recordings in California (Fletcher et al. 1984; Housner and Trifunac 1967; Trifunac and Hudson 1971; Trifunac 1972 b, c; Trifunac et al. 1998) and in Taiwan (Chen et al. 2001). In view of the fact that the data we use in this paper can provide only rough estimates of strong motion amplitudes at the earthquake source by means of extrapolation involving great distances between the areas where the data is recorded and the corresponding earthquake sources (especially for the HKS and IBS), it is interesting to note that the trends we find in this paper are in fair agreement with the data trends in California, which are based on recorded strong motion data there.

The slight trends seen in the $v_{\max}$ data where high values are underestimated and low amplitudes are overestimated (see Figures 4c, 5c, 6c, 7c and 8c) are another indicator that the form of attenuation equation in Equation (1) may call for additional higher-order terms. This trend may contribute to underestimates of σ in Figures 11 and 12 in terms of $v_{\max}$. A similar trend is also seen in Figure 9 that suggests a low growth rate of $d_{\max}$ with magnitude. We leave a detailed analysis of such trends and the development of more refined scaling equations for one of our future papers.

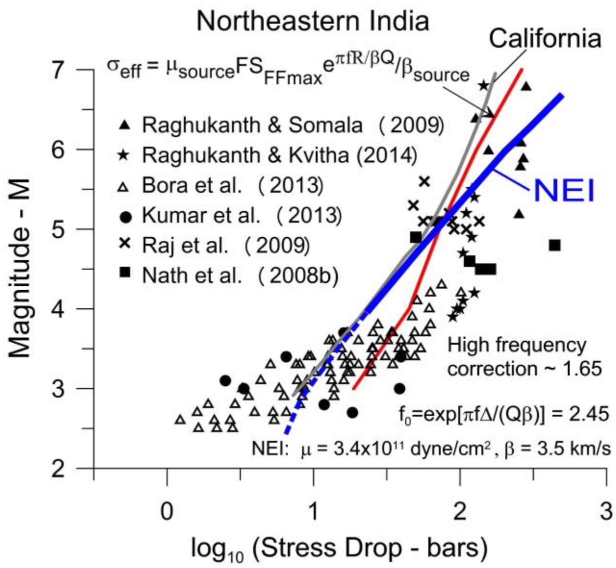

Fig. 12 A comparison of the stress-drop trend vs. versus magnitude (wide blue line for magnitudes between 4 and 6.75) based on $v_{\max} \sim \sigma\beta/\mu$ with the peak velocities for different magnitudes at the fault surface estimated for the NEI in this paper by extrapolation of regressed attenuation equation for $v_{\max}$, with (a) independent estimates of published values of stress drop by different investigators, (b) with average trends in California, and (c) with estimates of σ_{eff} based on empirical scaling model for Fourier Spectra (FS) by Gupta and Trifunac (2017)

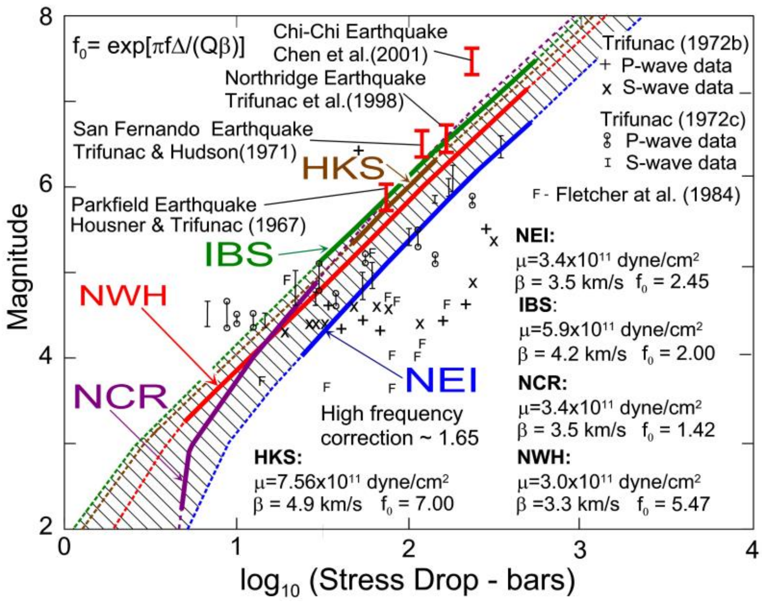

Fig. 13 A comparison of estimated trends for stress drop vs. magnitude (based on $v_{\max} \sim \sigma\beta/\mu$), at sources in the NWH, NEI, NCR, HKS and IBS with the stress-drop in California. Solid, wide lines show the trends for the intervals of magnitudes for which the data is available in this paper

CONCLUSIONS

In this paper we have presented empirical scaling equations for peak accelerations, velocities, and displacements of strong earthquake ground motion in five source-to-recording area regions of India (Figure 1b): the NWH for earthquakes that occur in Northwest Himalaya and are recorded in the same region, the NEI for earthquakes that occur in Northeast India and are recorded in the same region, the NCR for earthquakes that occur in the National Capital Region and are recorded in the same region, the IBS for earthquakes in the Burmese subduction zone and are recorded by stations in Northeast India, and the HKS for earthquakes that occur in the Hindu Kush and are recorded by stations in Northwest Himalaya. The five scaling equations describe different attenuations, which are representative of the specific source-path-recording station configurations. These equations complement our scaling equations for Fourier and pseudo-relative velocity spectra, which we developed for the same five regions (Gupta and Trifunac 2017, 2018 a, b, c, 2019). The scaling equations for peak velocities will make it possible to develop (a) hazard maps and (b) microzonation maps for extensions of response spectral amplitudes to include the effects of pseudo-static deformations caused by differential ground motion, and (c) for the design of underground structures that are sensitive to earthquake-induced strains.

REFERENCES

1. Anbazhagan, P., Kumar, Abhishek and Sitharam, T.G. (2013). “Ground Motion Prediction Equation Considering Combined Dataset of Recorded and Simulated Ground Motions”, *Soil Dynamics and Earthquake Engineering*, Vol. 53, pp. 92–108.
2. Bhat, G.M., Pandita, S.K., Singh, Y. and Sharma, S. (2013). “Source Parameters of Local Earthquakes in Jammu and Kashmir”, India, *Int. Jour. Scientific and Research Publications,* Vol. 3, No. 2, ISSN 2250-3153.
3. Bora, D.K., Baruah, S., Biswas, R. and Gogoi, N.K. (2013). “Estimation of Source Parameters of Local Earthquakes Originated in Shillong-Mikir Plateau and its Adjoining Region of Northeastern India”, *Bulletin of the Seismological Society of America*, Vol. 103, No. 1, pp. 437-446.
4. Borah, K., Kanna, N., Rai, S.S. and Prakasam, K.S. (2015). “Sediment Thickness Beneath the Indo-Gangetic Plain and Siwalik Himalaya Inferred from Receiver Function Modeling”, *Journal of Asian Earth Sciences*, Vol. 99, pp. 41–56.

5. Borgohain, J.M., Borah, K. and Bora, D.K. (2018). "Sediment Thickness Beneath Shillong-Mikir Plateau and its Adjoining Region of Northeast India Inferred from Tele seismic Receiver Function Modelling", *Himalayan Geol*ogy, Vol. 39, No. 1, pp. 47-56.
6. Chandrasekaran, A.R. and Das, J.D. (1993). "Strong Earthquake Ground Motion Data in EQINFOS for India: Part 1B", *Report No. CE 93-04, Dept. of Civil Eng., Univ. of Southern California, USA* (Edt. By M.D. Trifunac, M.I. Todorovska and V.W. Lee).
7. Chen, K-C., Huang, B-S., Wang, J-H., Huang, W-G., Chang, T-M., Hwang, R-D., Chiu, H-C., and Tsai, C-C. (2001). "An Observation of Rupture Pulses of the 20 September 1999 Chi-Chi, Taiwan, Earthquake from Near-Field Seismograms", *Bull. Seism. Soc. Amer.*, Vol. 91, No. 5, pp. 1247–1254.
8. Chopra, S., Kumar, V., Suthar, A. and Kumar, P. (2012). "Modeling of Strong Ground Motions for 1991 Uttarkashi, 1999 Chamoli Earthquakes and a Hypothetical Great Earthquake in Garhwal-Kumaun Himalaya", *Nat. Hazards*, Vol. 64, pp. 1141-1159.
9. Douglas, J. (2003). "Earthquake Ground Motion Estimation Using Strong Motion Records: a Review of Equations for Estimation of Peak Ground Acceleration and Response Spectral Ordinates", *Earth Science – Reviews*, Vol. 61, pp. 43-104.
10. Douglas, J. (2017). "Ground Motion Prediction Equations 1964–2016", Report, *Department of Civil and Environmental Engineering, University of Stratchlyde*, Glasgow, U.K (available online at www.gmpe.org.wk/gmpereport2014.pdf).
11. Douglas, J. and Aochi, H. (2008). "A Survey of Techniques for Predicting Earthquake Ground Motions for Engineering Purposes", *Surv. Geophys.*, Vol. 29, pp. 187-230.
12. Fletcher, J., Boatwright, J., Haar, L., Hanks, T. and McGarr, A. (1984). "Source Parameters for Aftershocks of the Oroville, California, Earthquake", *Bull. Seismological Soc. of America*, Vol. 74, No. 4, pp. 1101–1123.
13. Gičev, V. and Trifunac, M.D. (2022). "High Frequency Decay of the Fourier Spectra of Strong Motion Acceleration", *Earthquake Engineering and Resilience*, Vol. 1, No. 3, pp. 302 - 316.
14. Gupta, I.D. (2018). "Uniformly Processed Strong Motion Database for Himalaya and Northeast Region of India", *Pure and Appl. Geophysics*, Vol. 175, No. 3, pp. 829-863, DOI 10.1007/s00024-017-1703-y
15. Gupta, I.D. (2024). "Probabilistic Fault Displacement Hazard Analysis (PFDHA) for a Strand of Main Boundary Thrust (MBT) in Garhwal-Kumaon Himalaya", *Int. J. Adv. Eng. Sci. Appl. Math.*, Vol. 16, pp. 199–219, https://doi.org/10.1007/s12572-023-00359-y
16. Gupta, I.D. and Trifunac, M.D. (2017). "Scaling of Fourier Spectra of Strong Earthquake Ground Motion in Western Himalaya and Northeastern India", *Soil Dynamics and Earthquake Engineering*, Vol. 106, pp. 137-159.
17. Gupta, I.D. and Trifunac, M.D. (2018a). "Empirical Scaling Relations for Pseudo Relative Velocity Spectra in Western Himalaya and Northeast India", *Soil Dynamics and Earthquake Engineering*, Vol. 106, pp. 70-89.
18. Gupta, I.D. and Trifunac, M.D. (2018b). "Attenuation of Strong Earthquake Ground Motion – II: Dependence on Geology Along the Wave Paths from the Burmese 5 Zone to Northeastern India", *Soil Dynamics and Earthquake Engineering*, Vol. 112, pp. 256-276.
19. Gupta, I.D. and Trifunac, M.D. (2018c). "Attenuation of Strong Earthquake Ground Motion – I: Dependence on Geology Along the Wave Paths from the Hindu Kush Subduction Zone to Western Himalaya", *Soil Dynamics and Earthquake Engineering*, Vol. 114, pp. 127-145.
20. Gupta, I.D. and Trifunac, M.D. (2019). "Attenuation of Fourier Amplitude and Pseudo Relative Velocity Spectra due to Local Earthquakes in the National Capital Region of India", *Soil Dynamics and Earthquake Engineering*, Vol. 116, pp. 593-611.
21. Gusev, A.A. (1983). "Descriptive Statistical Model of Earthquake Source Radiation and its Application to an Estimation of Short-Period Strong Motion", *Geological J. Royal Astro. Soc*., Vol. 74, pp. 787-808.
22. Harbindu, A., Kamal and Sharma, M.L. (2012). "Site Amplification and Frequency-Dependent Attenuation Coefficient at Rock Sites of the Himachal Region in Northwest Himalaya, India", *Bull. Seism. Soc. of Am.*, Vol. 102, No. 4, pp. 1497-1504.
23. Housner, G.W., and Trifunac, M.D. (1967). "Analysis of Accelerograms—Parkfield Earthquake", *Bull. Seism. Soc. Amer*., Vol. *57, No.* 6, pp. 1193–1220.
24. Hudson, D.E. (1979). "Reading and Interpreting Strong Motion Accelerograms", *Earthquake Engineering Research Institute*.

25. Joshi, A., Mohanty, M., Bansal, A.R., Dimri, V.P. and Chadha, R.K. (2010). "Use of Strong-Motion Data for Frequency-Dependent Shear Wave Attenuation Studies in the Pithoragarh Region of Kumaon Himalaya", *ISET Jour. Earthq. Tech*., Paper No. 508, Vol. 47, No. 1, pp. 25–46.
26. Joshi, A., Mohanty, P.M., Bansal, A.R., Dimri, V.P. and Chadha, R.K. (2012). "Determination of $Q_\beta(f)$ in Different Parts of Kumaon Himalaya from the Inversion of Spectral Acceleration Data", *Pure Appl. Geophys.*, Vol. 169, No. 10, pp. 1821-1845.
27. Kumar, A., Kumar, A., Gupta, S.C., Mittal, H. and Kumar, R. (2013). "Source Parameters and f_{max} in Kameng Region of Arunachal Lesser Himalaya", *Journal of Asian Earth Sciences*, Vol. 70-71, pp. 35-44.
28. Kumar, A., Sinvhal, A., Joshi, A., Kumar, D., Sandeep and Kumar, P. (2015). "Coda Wave Attenuation Characteristics for Kumaon and Garhwal Himalaya, India", *Nat. Hazards*, Vol. 75, pp. 1057–1074.
29. Lee, V.W., Trifunac, M.D., Todorovska, M.I and Novikova, E.I. (1995). "Empirical Equations Describing Attenuation of the Peaks of Strong Ground Motion, in terms of Magnitude, Distance, Path Effects and Site Conditions", *Civil Eng. Report CE 95-02, Univ. of Southern Cal.*, Los Angeles.
30. Malhotra, P.K. (2006). "Smooth Spectra of Horizontal and Vertical Ground Motions", *Bull Seism Soc Am*., Vol. 96, No. 2, pp. 506–518.
31. Mohanty, W.K., Prakash, R., Suresh, G., Shukla, A.K., Aalling, M.Y.W. and Srivastava, J.P. (2009). "Estimation of Coda Wave Attenuation for the National Capital Region, Delhi, India Using Local Earthquakes", *Pure and Applied Geophysics*, Vol. 166, No. 3, pp. 429-449.
32. Nath, S.K., Shukla, K. and Vyas, M. (2008a). "Seismic Hazard Scenario and Attenuation Model of the Garhwal Himalaya Using Near-Field Synthesis from Weak Motion Seismometry", *J. Earth Syst. Sci.*, Vol. 117 (S2), pp. 649-670.
33. Nath, S.K., Raj, A., Sharma, J., Thingbaijam, K.K.S., Kumar, A., Nandy, D.R., Yadav, M.K., Dasgupta, S., Majumdar, K., Kayal, J.R., Shukla, A.K., Deb, S.K., Pathak, J., Hazarika, P.J., Paul, D.K. and Bansal, B.K. (2008b). "Site Amplification, Q_s, and Source Parameterization in Guwahati Region from Seismic and Geotechnical Analysis", *Seismologica Research Letters*, Vol. 79, No. 4, pp. 526-539.
34. Raghucharan, M.C., Somala, S.N. and Rodina, S. (2019). "Seismic Attenuation Model Using Artificial Neural Networks", *Soil Dyn. Earthq. Eng*., Vol. 126, pp. 105828.
35. Raghukanth, S.T.G. and Somala, S.N. (2009). "Modeling of Strong-Motion Data in Northeastern India: Q, Stress Drop, and Site Amplification", *Bulletin Seismological Society of America*, Vol. 99, No. 2A, pp. 705-725.
36. Raghukanth. S.T.G. and Kavitha, B. (2014). "Ground Motion Relations for Active Regions in India", *Pure and Applied Geophysics*, DOI 10.1007/s00024-014-0807-x.
37. Raj, A., Nath, S.K., Bansal, B.K., Thingbaijam, K.K.S., Kumar, A., Thiruvengadam, N., Yadav, A. and Arrawatia, M.L. (2009). "Rapid Estimation of Source Parameters Using Finite Fault Modeling – Case Studies from the Sikkim and Garhwal Himalayas", *Seismological Research Letters*, Vol. 80, No. 1, pp. 89-96.
38. Ramkrishnan, R., Kolathayar, S. and Sitharam, T.G. (2021). "Development of New Ground Motion Prediction Equation for the North and Central Himalayas Using Recorded Strong Motion Data", *Jour. Earthq. Eng.*, Vol. 25, No. 10, pp. 1903-1926.
39. Saikia, S., Chopra, S., Baruah, S. and Singh, U.K. (2016). "Shallow Sedimentary Structure of the Brahmaputra Valley Constraint from Receiver Functions Analysis", *Pure Appl. Geophys*., Vol. 174, pp. 229-247.
40. Searle, M., Hacker, B.R. and Bilham, R. (2001). "The Hindu Kush Seismic Zone as a Paradigm for the Creation of Ultrahigh-Pressure Diamond- and Coesite-Bearing Continental Rocks", *J. of Geology*, Vol. 109, pp. 143-153.
41. Sharma, M.L. and Wason, H.R. (1994). "Occurrence of Low Stress Drop Earthquakes in the Garhwal Himalaya Region", *Physics of Earth and Planetary Interior*, Vol. 85, pp. 265-272.
42. Sharma, M.L., Douglas, J., Bungam, H. and Kotadia, J. (2009). "Ground-Motion Prediction Equations Based on Data from the Himalayan and Zagros Regions", *Jour. Earthq. Eng.*, Vol. 13, No. 8, pp. 1191-1210.
43. Sharma, J., Chopra, S., and Roy, K.S. (2014). "Estimation of Source Parameters, Quality Factor (Qs), and Site Characteristics Using Accelerograms: Uttarakhand Himalaya region", *Bull. Seism. Soc. Am.*, Vol. 104, No. 1, pp. 360-380.

44. Thatcher, W. and Hanks, T.C. (1973). "Source Parameters of Southern California Earthquakes", *J. Geoph. Res.*, Vol. 78, pp. 8547-8576.
45. Todorovska, M.I and Trifunac, M.D. (1996a). "Hazard Mapping of Normalized Peak Strain in Soil During Earthquakes - Microzonation of a Metropolitan Area", *Soil Dynamics and Earthquake Eng.*, Vol. 15, No. 5, pp. 321-329.
46. Todorovska, M.I and Trifunac, M.D. (1996b). "A Seismic Hazard Model for Peak Strains in Soils During Strong Earthquake Shaking", *Earthquake Engineering and Engineering Vibration*, Vol. 16, Supplement, pp. 1-12.
47. Todorovska, M.I., Trifunac, M.D. and Lee, V.W. (2007). "Shaking Hazard Compatible Methodology for Probabilistic Assessment of Permanent Ground Displacement Across Earthquake Faults", *Soil Dyn. & Earthq. Eng.*, Vol. 27, pp. 586–597.
48. Trifunac, M.D. (1972a). "A Note on Correction of Strong-Motion Accelerograms for Instrument Response", *Bull. Seism. Soc. Amer*., Vol. 62, No. 1, pp. 401-409.
49. Trifunac, M.D. (1972b). "Stress Estimates for San Fernando, California Earthquake of February 9, 1971: Main Event and Thirteen Aftershocks", *Bull. Seism. Soc. Amer.*, Vol. 62, No. 3, pp. 721–750.
50. Trifunac, M.D. (1972c). "Tectonic Stress and Source Mechanism of the Imperial Valley, California Earthquake of 1940", *Bull. Seism. Soc. Amer.*, Vol. 62, No. 5, pp. 1283–1302.
51. Trifunac, M.D. (1987). "Influence of Local Soil and Geologic Site Conditions on Fourier Spectrum Amplitudes of Recorded Strong Motion Accelerations", *Report CE 87-04, University of Southern* California, Los Angeles, USA.
52. Trifunac, M.D. and Anderson, J.G. (1977). "Preliminary Empirical Models for Scaling Absolute Acceleration Spectra", *Report CE 77-03, University of Southern California*, Los Angeles, USA.
53. Trifunac, M.D. and Brady, A.G. (1975). "On the Correlation of Seismic Intensity Scales with the Peaks of Recorded Strong Ground Motion", *Bull. Seism. Soc. Amer*., Vol. 65, No. 1, pp. 139-162.
54. Trifunac, M.D. and Brady, A.G. (1976). "Correlations of Peak Acceleration, Velocity and Displacement with Earthquake Magnitude, Epicentral Distance and Site Conditions", *Intl. J. of Earthquake Engineering and Struct. Dynamics,* Vol. 4, No. 5, pp. 455-471.
55. Trifunac, M.D. and Gičev, V. (2006). "Response Spectra for Differential Motion of Columns, Paper II: Out-of-Plane Response", *Soil Dynamics and Earthquake Engineering,* Vol. 26, No 12, pp. 1149-1160.
56. Trifunac, M.D. and Hudson, D.E. (1971). "Analysis of the Pacoima Dam accelerogram, San Fernando, California earthquake of 1971", *Bull. Seism. Soc. Amer*., Vol. 61, No. 5, pp. 1393–1411.
57. Trifunac, M.D. and Lee, V.W. (1996). "Peak Surface Strains During Strong Earthquake Motion", *Soil Dynamics and Earthquake Eng*., Vol. 15, No. 5, pp. 311-319.
58. Trifunac, M.D., and Todorovska, M.I. (1997). "Response Spectra and Differential Motion of Columns", *Earthquake Eng. and Structural Dyn*., Vol. 26, No. 2, pp. 251-268.
59. Trifunac, M.D., Todorovska, M.I. and Ivanovic, S. (1996). "Peak Velocities, and Peak Surface Strains During Northridge, California, Earthquake of 17 January 1994", *Soil Dynamics and Earthquake Eng.*, Vol. 15, No. 5, pp. 301-310.
60. Trifunac, M.D., Todorovska, M.I. and Lee, V.W. (1998). "The Rinaldi Strong Motion Accelerogram of the Northridge, California, Earthquake of 17 January 1994", *Earthquake Spectra 1998,* Vol. 14, No. 1, pp. 225–239.
61. Trifunac, M.D., Jalali, R.S., Todorovska, M.I. and Kisomi, B. (2020). "The Contribution of Cord Rotations to Structural Response", *Soil Dynamics and Earthquake Engineering*, Vol. 139, pp. 106351.
62. Vandana, S., Gupta, C. and Kumar, A. (2015). "Coda Wave Attenuation Characteristics for the Bilaspur Region of Himachal Lesser Himalaya", *Nat Hazards*, Vol. 78, pp. 1091–1110.
63. Wang, C., Dai, J., Zhao, X., Li, Y., Graham, S.A., He, D., Ran, B. and Meng, J. (2014). "Outward-growth of the Tibetan Plateau during Cenozoic: A Review", *Tectonophysics*, Vol. 621, pp. 1-43.
64. Wason, H.R. and Sharma, M.L. (2000). "Source Parameters Study of Local Earthquakes in the Garhwal Himalaya Region Based on the Digital Broadband Data", *Procs. 10th World Conference on Earthquake Engineering*.
65. Wu, R. and Aki, K. (1988). "Multiple Scattering and Energy Transfer of Seismic Waves - Separation of Scattering Effect from Intrinsic Attenuation II. Application of the theory to Hindu Kush region", *Pure Appl Geophys,* Vol. 128, No. 1, pp. 49–80.